A99-33643

AIAA 99-3582

Compressibility Effects on Entrainment and Mixing in Supersonic Planar Turbulent Wakes

Masaki Nakagawa and Werner J.A. Dahm

Laboratory for Turbulence and Combustion (LTC)
Department of Aerospace Engineering
The University of Michigan
Ann Arbor, MI

30th AIAA Fluid Dynamics Conference
28 June - 1 July, 1999 / Norfolk, VA

AIAA Paper No. 99-3582 presented at the 30th AIAA Fluid Dynamics Conference, 28 June - 1 July 1999, Norfolk, VA.

Compressibility Effects on Entrainment and Mixing in Supersonic Planar Turbulent Wakes

Masaki Nakagawa[1] and Werner J.A. Dahm[2]

Laboratory for Turbulence and Combustion (LTC)
Department of Aerospace Engineering
The University of Michigan
Ann Arbor, MI 48109-2140

Results are presented from an experimental investigation of compressibility effects on entrainment and mixing in the near- and far-fields of a supersonic, planar, turbulent, bluff-body wake formed by a two-dimensional slot jet nozzle aligned with a Mach 1.6 free stream. Planar laser Mie scattering (PLMS) and shadowgraph/schlieren imaging are combined with pitot and static pressure measurements to examine the mean flow scaling laws and the instantaneous structure of the near- and far-fields. Results show a classical vortex street-like large-scale structure in the wake far field, where the relative Mach number has decreased to clearly subsonic values. Where the relative Mach number is transonic, the far-field growth rate and velocity decay determined from PLMS imaging and mean velocity profiles follow the characteristic $(\delta/\vartheta) \sim (x/\vartheta)^{1/2}$ and $(u/U_\infty) \sim (x/\vartheta)^{-1/2}$ scaling of incompressible planar turbulent wakes. The virtual origin (x_0/ϑ) is shifted downstream as a result of the expansion and recompression in the base flow region, by an amount that depends on the flow rate from the nozzle. Interaction of the reflected recompression shock with the large-scale vortical structures in the wake produces quasi-periodic forcing that affects the constants in the local flow width scaling and velocity defect scaling. Results for the scaling constants in the present supersonic wake agree with values reported for forced incompressible wakes.

1. INTRODUCTIO N

Future airbreathing propulsion systems may involve supersonic combustors, in which a subsonic fuel stream must be mixed and burned with a supersonic airstream. Under such conditions, compressibility effects can significantly alter the entrainment and mixing processes from prior design experience in subsonic flows. To establish the technical background needed to develop supersonic combustors, research over the past decade has sought to clarify the effects of compressibility on mixing and combustion in turbulent shear flows. Two main avenues of work have been pursued toward this end. The first has examined entrainment and mixing in relatively complex configurations that approximate practical supersonic combustors (*e.g.*, Northam *et al* 1989, Nejad *et al* 1994). However many of these involve complications in both the geometry and the flow characteristics that limit the measurements obtained and prohibit detailed comparisons with other flows. The second approach studies elementary turbulent shear flows under more precisely controllable conditions to develop a fundamental understanding of compressibility effects on entrainment and mixing, which can then be applied to a wide range of practical configurations.

As regards the latter, the most widely studied flow has been the turbulent mixing layer. Its relative simplicity and the extensive documentation of its large-scale structure and dynamics under incompressible flow conditions make it well suited for this purpose, and several specific effects of compressibility have been observed in supersonic mixing layers. These include changes in the similarity scaling properties of the flow, in particular a reduction in growth rate with increasing convective Mach number and an attendant reduction in entrainment and mixing rates, as well as changes in the structure and dynamics of the large scales, including a loss of two-dimensionality of the large-scale structures (*e.g.*, Dimotakis 1991). Many of these phenomena are currently believed to be generic effects of compressibility in turbulent shear flows, and thus are expected to be found in an analogous form in other turbulent shear flows under locally supersonic flow conditions.

However, at least some of these effects of compressibility seen in mixing layers are likely to result from the particular large-scale structure and dynamics of that turbulent shear flow. It appears likely that flows with other scaling properties, and therefore other large-scale structure characteristics, may demonstrate some of the compressibility effects seen in mixing layers, but may also show certain other phenomena not seen in mixing layers.

With this motivation, we present results from an experimental investigation into the effects of compressibility on the large-scale structure and associated entrainment and mixing properties in a supersonic, planar, turbulent, bluff-body wake. These are compared with results from incompressible wakes and with corresponding results from supersonic mixing layers to identify generic effects of compressibility on the entrainment and mixing properties of turbulent shear flows.

Incompressible planar turbulent wakes generated by bluff bodies are by now reasonably well understood (*e.g.*, Wygnanski *et al* 1986). However, most studies of supersonic bluff-body wakes have focused almost entirely on the base flow region (*e.g.*, Chapman 1951, Amatucci *et al* 1992, Herrin & Dutton 1994). Recent experiments by Lachney *et al* (1995) and Lachney & Clemens (1998) give laser imaging results for the mean pressure

[1] Graduate Student; AIAA Student Member.
[2] Professor; AIAA Senior Member; Corresponding author.

and temperature fields in the near-wake region of supersonic bluff-body wakes. Clemens *et al* (1996) and Clemens & Smith (1998) present observations of transition and the development of large-scale structures in a supersonic slender-body wake formed by laminar boundary layers merging at the sharp end of a thin, tapered splitter plate, without any bluff body recirculation zone. Chen *et al* (1990) conducted direct numerical simulations of stability and transition in time-developing supersonic wakes with no bluff-body, and found large scale structures similar to those in incompressible wakes.

However to date there have been no detailed studies of the supersonic bluff-body turbulent wake that span from the base flow region well into the self-similar far-field wake flow region. The present study focuses primarily on imaging results for the instantaneous large scale structure and mean scaling properties of two-dimensional, supersonic, turbulent, bluff-body wakes, and makes comparisons with incompressible wakes to identify effects of compressibility.

2. FACILITY AND DIAGNOSTICS

The experiments reported here were conducted in a Supersonic Mixing and Combustion Tunnel designed specifically for studies of supersonic coflowing turbulent jets and wakes. The test section interior measured 34.6 mm × 38.4 mm in cross section and 553 mm in length. A subsonic slot nozzle having exterior dimensions of 4.2 mm × 38.4 mm and interior dimensions of 2.0 mm × 36.2 mm was centered in the test section entrance plane. As indicated in Figs. 1 and 2, the slot nozzle entered the

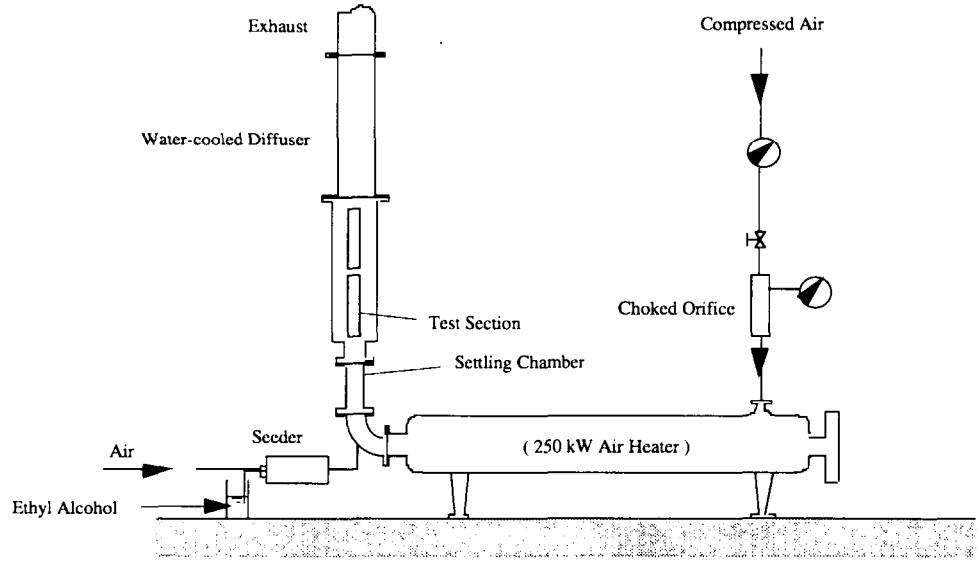

Figure 1. Schematic of the Michigan Supersonic Mixing and Combustion Tunnel, showing the test section, the electric air heater, the alcohol seeder, and the major components of the flow control system.

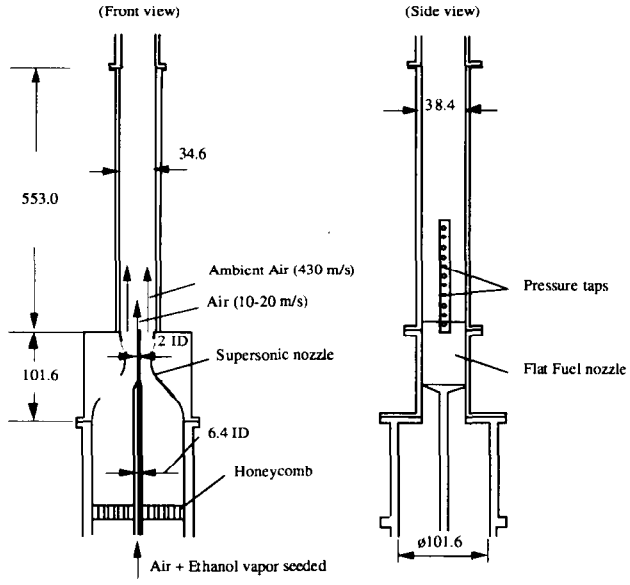

Figure 2. Schematic of the supersonic tunnel nozzle, the test section, and the subsonic slot nozzle showing side view *(left)* and plan view *(right)*. Dimensions are in mm.

tunnel through a 1/4-in. ID round tube, and then flattened in the lateral direction just upstream of the throat while expanding in the spanwise direction. The nozzle was packed with glass beads and screens beginning just past the expansion section and continuing through most of the 65 mm long parallel section to give a uniform low-speed flow (typically 10-20 m/s) across the exit plane of the slot. The present results are for air flow through the slot nozzle, in some cases with alcohol vapor seeding for visualization purposes.

The supersonic nozzle was designed with the NOZCS3 program from the University of Illinois to produce wave-free Mach 2.0 air flow in the presence of the slot nozzle. The throat area measured 9.0 mm × 38.4 mm on each side of the slot nozzle, and diverged to give an exit area of 15.2 mm × 38.4 mm on each side of the slot nozzle at the entrance to the test section. However, owing to the relatively small cross section of the tunnel, viscous boundary layers along the supersonic nozzle and tunnel sidewalls, and along the outer walls of the slot nozzle, produced a significant reduction in the effective cross sectional area of the tunnel. This lowered the Mach number entering the two sides of the test section to $M_\infty \approx 1.55$ and 1.59 as determined by the measured pressure ratios. This corresponds to a velocity and static temperature at the test section entrance of 430 m/s and 190 K, respectively, and a Reynolds number based on plate length from the throat of 2.1 (10^6).

The boundary layers on the outside of the slot nozzle produced a drag per unit span, D, that greatly exceeded the momentum per unit span, J, introduced by the flow through the slot nozzle.

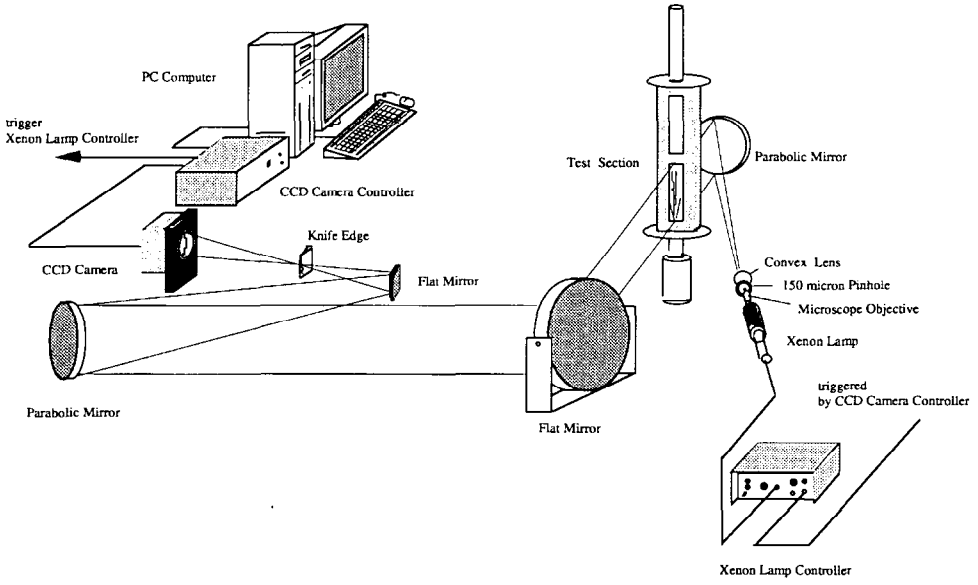

Figure 3. Schematic of the shadowgraph / schlieren imaging system.

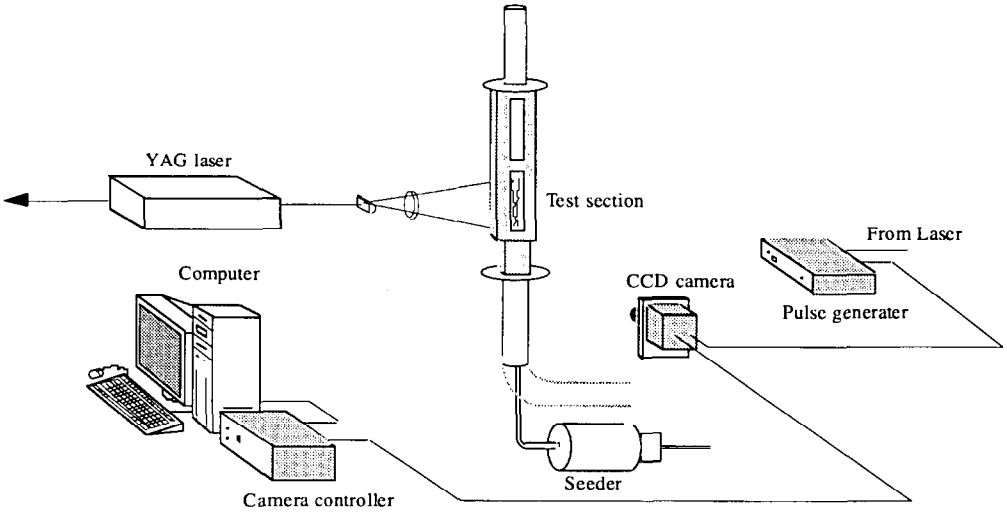

Figure 4. Schematic of the planar laser Mie scattering (PLMS) imaging system.

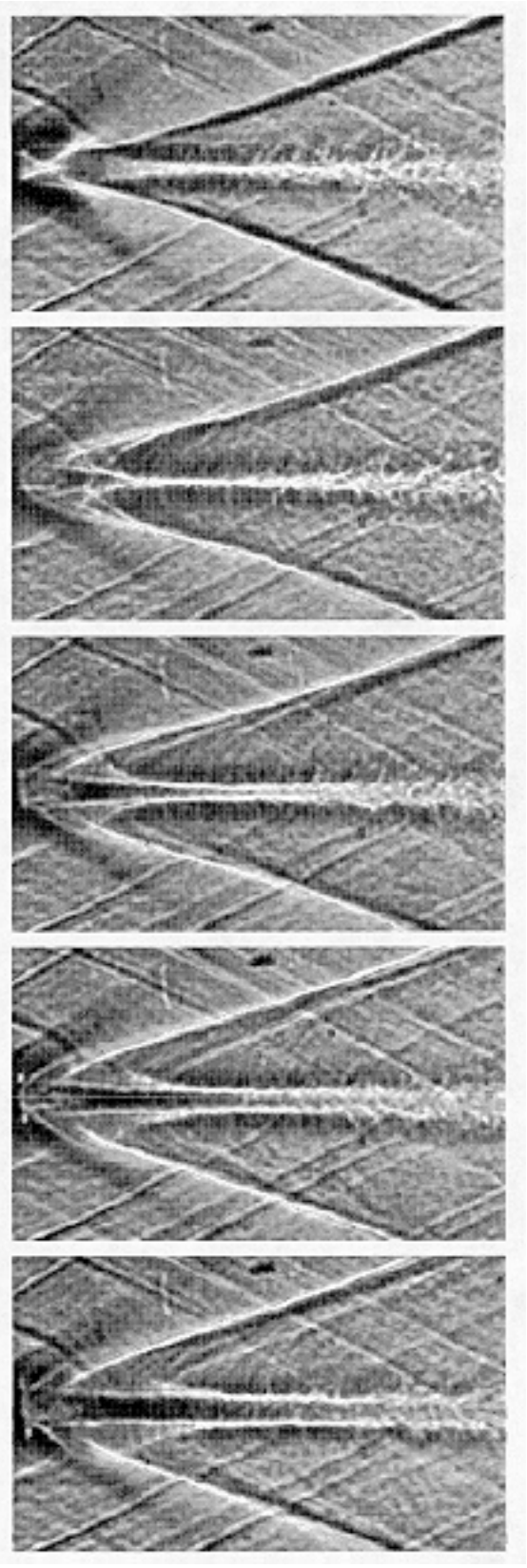

Figure 5. Shadowgraph images showing effect of slot jet flow rate as determined by jet supply pressure on wave pattern, near field structure, and near field length. Shown from top to bottom are results for 0 psi (no jet flow), 15 psi, 30 psi, 45 psi, and 60 psi. See also Figs. 12 and 14.

The nozzle thus acts as a bluff-body wake generator, with the flow through it serving mainly to permit visualization of the resulting turbulent wake. The net drag ($D - J$) produced a wake momentum thickness $\vartheta = 0.40 \pm 0.03$ mm as determined from velocity profiles measured in the self-similar far-field region.

The wall static pressure distribution was monitored with a total of 32 sidewall pressure taps. Sidewalls were kept parallel for all results reported here. Any variations in wall static pressure due to the displacement effect of the wake flow itself were negligible in comparison with variations induced by the repeated reflections of the wake expansion fan and recompression shock from the tunnel walls. Static and pitot pressures were measured on the wake centerline and across the flow, respectively, at several downstream locations with probes designed as recommended by Pope & Goin (1965). Pitot pressures were converted to total pressures using the Rayleigh supersonic pitot formula.

Schlieren and shadowgraph imaging (Fig. 3) were used to document the wave patterns in the near-field expansion and recompression region and throughout the test section. Light from a Xenon Corp. "Nanolamp" with 20 nsec pulse duration passed through a microscope objective with a 400 μm pinhole and was imaged onto a Princeton Instruments thermoelectrically cooled 512 × 512 CCD array.

Planar laser Mie scattering (PLMS) imaging (Fig. 4) was used to document the instantaneous structure and growth rate of the flow. Alcohol vapor was introduced in the air issuing from the slot nozzle by spraying ethanol approximately 1 m upstream of the nozzle in a seeder. The alcohol vaporizes in the air stream before exiting the nozzle, with the resulting mass fraction of alcohol being approximately 1%. When the alcohol vapor mixes with the cold, supersonic, free stream air in the test section, it condenses to form a fine fog. Light in a thin laser sheet formed from an Nd:YAG laser with 10 nsec pulse duration, which passes through the wake, is then Mie scattered from the fog and imaged onto the same CCD array.

3. FLOW VISUALIZATION RESULTS

3.1 Base Flow Region

Figure 5 shows magnified shadowgraph images of the base flow region immediately downstream of the slot jet nozzle for various

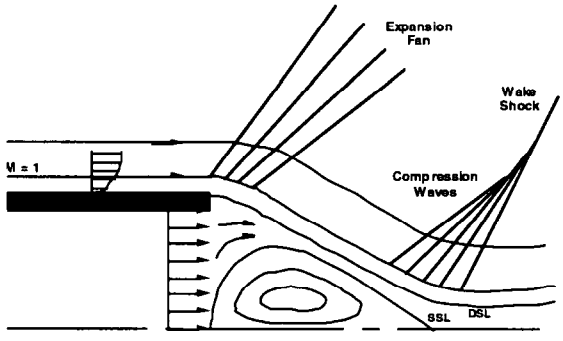

Figure 6. Schematic indicating major features of supersonic base flow region just beyond slot jet exit, showing wake expansion and recompression waves above wake centerline, as well as coupling between slot jet flow rate and base flow structure and size.

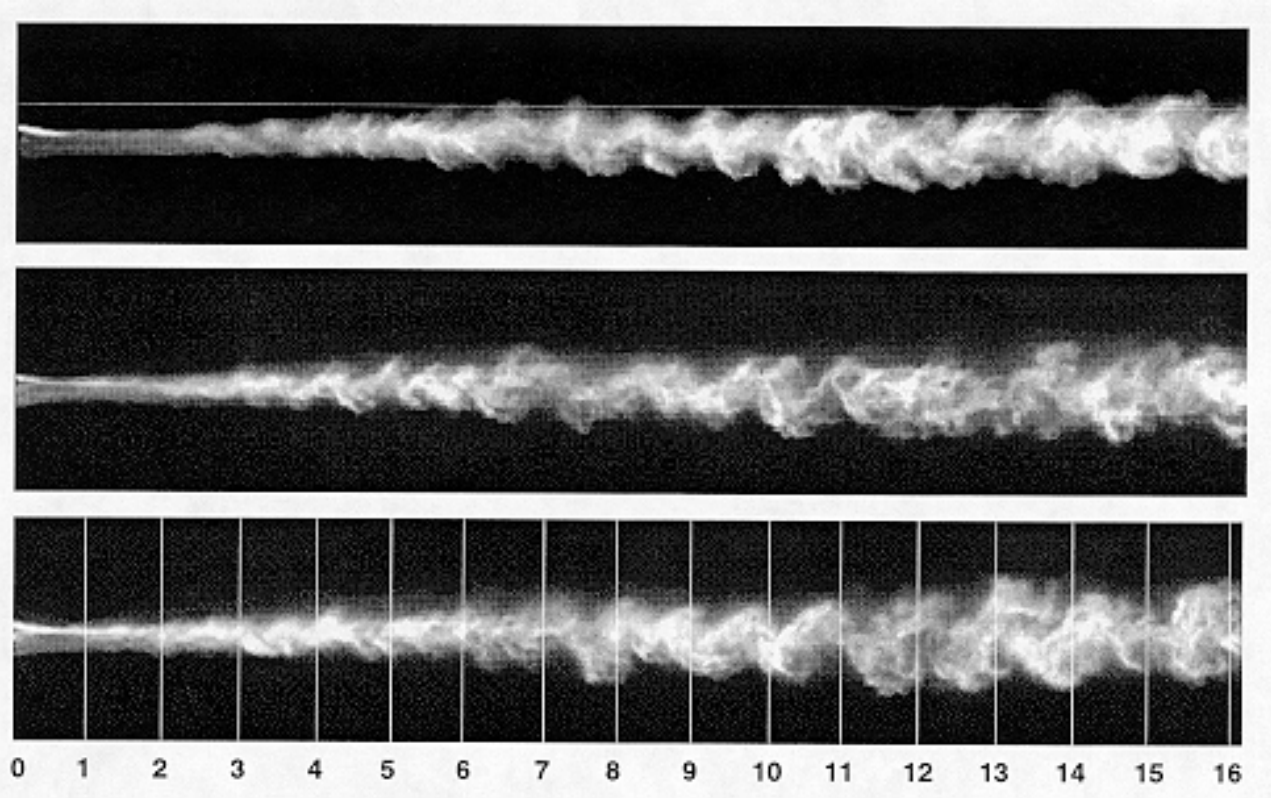

Figure 7. Typical instantaneous PLMS images showing structure in the supersonic, planar, turbulent wake flow. Note development of characteristic vortex street-like large scale structures in far field, with alternating signs of circulation, and the lack of any apparent structures immediately downstream of base flow region, where the relative Mach number remains high. Scale at bottom shows distance x (cm) beyond jet nozzle.

jet flow rates. In the top panel, where there is no flow through the nozzle, the expansion and recompression process in the base flow region is seen to occur within a relatively short distance past the nozzle exit. In the remaining panels, corresponding to increasing volume flow rates through the nozzle, the base flow region becomes much longer and the compression wave is seen to broaden considerably. At high flow rates, the recompression shock is seen to become weaker. The expansion wave presumably also weakens, since the volume displaced by the inflow requires the free stream to be turned through a smaller angle.

These observations are consistent with the schematic in Fig. 6, which shows the major features of the classical two-dimensional supersonic base flow with mass injection (*e.g.*, Berger 1971). The free shear layers resulting from the separated boundary layers are turned by an expansion fan through the angle required to match the base pressure, which in this case is related to the jet flow rate in Fig. 5. The shear layers merge near the centerline, where compression waves realign the flow more or less with the free stream. The compression waves coalesce into a wake shock, and in general will interact with the expansion fan. Without injection through the jet nozzle, the extent of the base flow region is set by the slot width. With injection, the stagnation streamline and the dividing streamline in the base flow separate to accommodate the volume flow rate. The resulting displacement effect reduces the angle through which the expansion fan must turn the flow, and thereby causes the base flow region to extend further downstream. Through this mechanism, it can be anticipated that the jet flow rate will affect the virtual origin of the resulting far-field wake flow.

3.2 Far-Field Region

The volume flow rate through the jet nozzle used for the PLMS visualizations corresponds roughly to the second panel in Fig. 5. Figure 7 shows three typical examples of the resulting instantaneous PLMS images, spanning from the nozzle exit well into the wake far field. The comparatively steady base flow region discussed above can be seen at the extreme left side of these images. At about x = 3 cm downstream of the jet nozzle (*i.e.*, around $x/\vartheta \approx 75$), large-scale organized vortical structures with alternating signs of circulation can be seen to begin forming. By about x = 6 cm, corresponding to $x/\vartheta \approx 150$, these structures typically have organized into a characteristic, quasi-periodic, vortex street-like pattern that continues downstream. The wake can be seen to broaden slowly with increasing downstream distance. The size and spacing of the vortical structures appears to increase with the wake width.

Figure 8 shows the ensemble-average of 92 instantaneous PLMS images of the type in Fig. 7. The mean growth of the wake can be readily seen. The slightly darker regions near x = 7

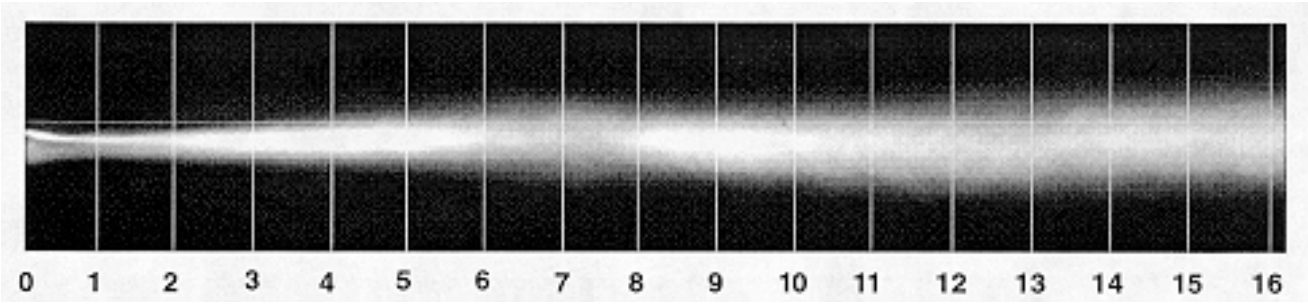

Figure 8. Ensemble-averaged PLMS image for the supersonic, planar, turbulent wake flow. Scale gives distance from the jet nozzle in cm. Dark regions coincide with reflected shock interactions seens in Fig. 9. Lateral profiles of mean intensity are shown in Fig. 11.

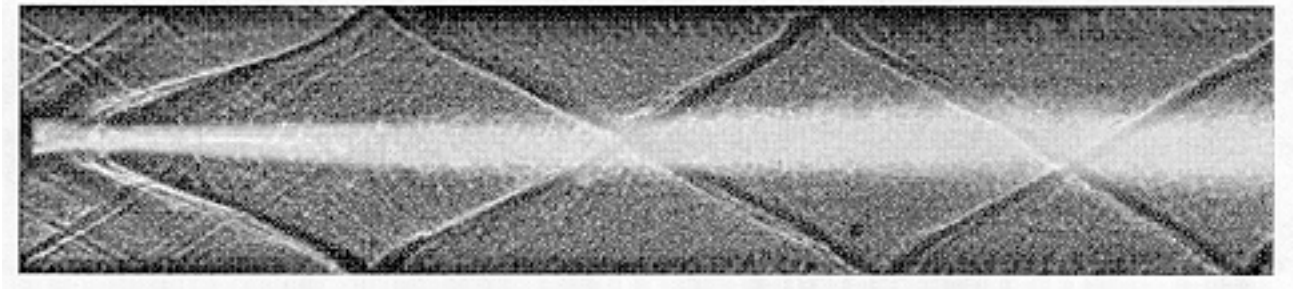

Figure 9. Instantaneous shadowgraph image, showing wave structure for parallel sidewalls, with mean PLMS image from Fig. 8 superimposed. Measured wall static pressure distribution is shown in Fig. 10.

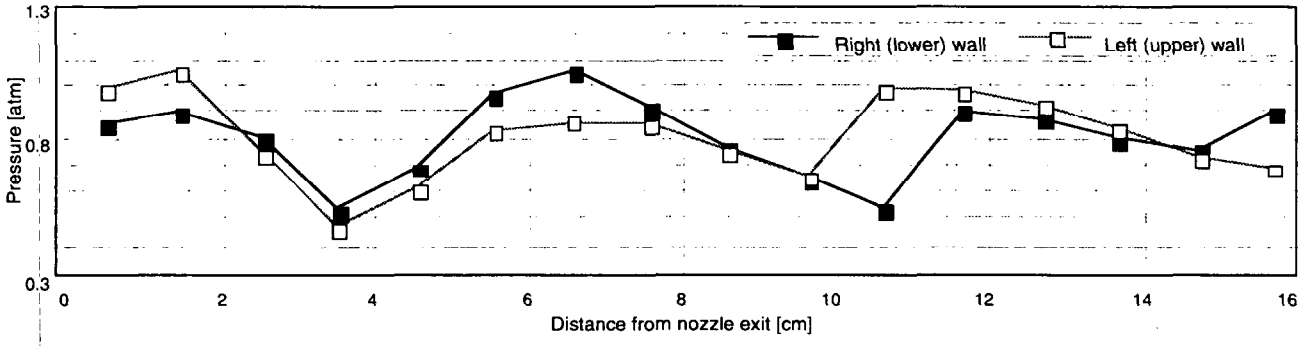

Figure 10. Measured wall static pressure distribution, giving pressure (in atm) against downstream distance (in cm). Compare with wave patterns at sidewalls in Fig. 9. Expansion fan and its reflections from sidewalls lead to smooth pressure variations along walls.

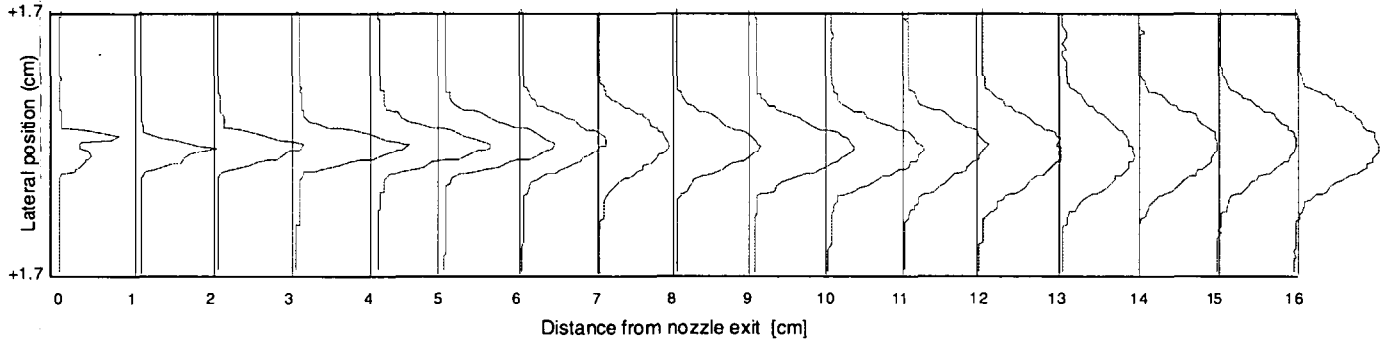

Figure 11. Lateral profiles of the relative intensity in mean PLMS image in Fig. 8 (in arbitrary units) against downstream distance (in cm). Key interest is in examining compressibility effects on the local profile widths $\delta(x)$ versus downstream distance x; see §5.1.

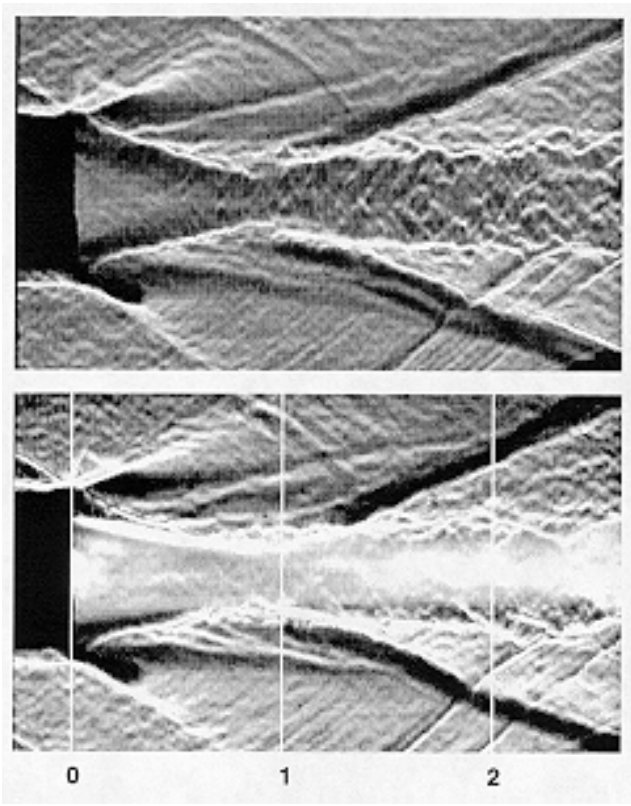

Figure 12. Shadowgraph images of near field region *(upper)* and with typical jet PLMS image superimposed *(lower)*, showing base flow region and early self-similar wake. Scale gives x in cm.

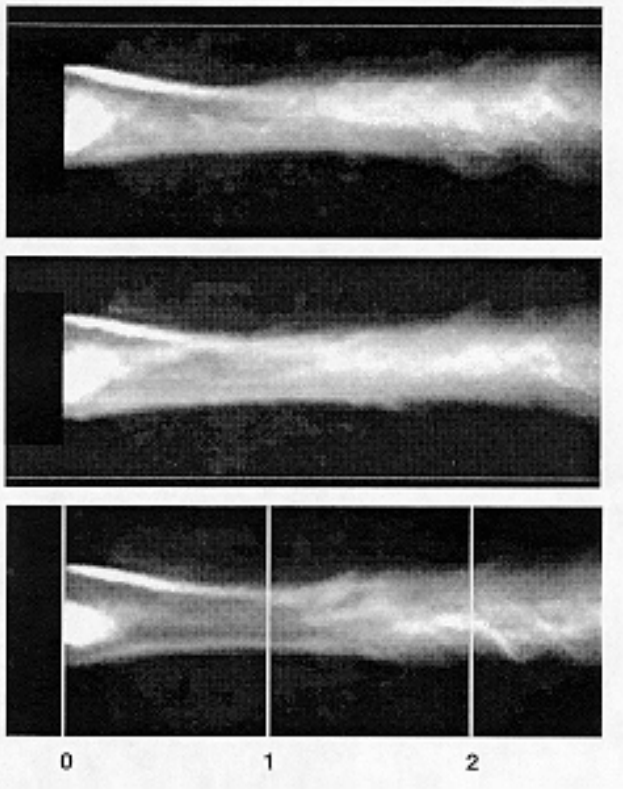

Figure 13. Three typical instantaneous PLMS images in the jet near field region. No organized vortical structures have formed up to the right edge of the field of view. Scale gives x in cm.

cm and 13 cm coincide with interactions between the flow and reflections of the wake shock from the tunnel sidewalls. The wake is also deflected slightly after each of these shock interactions, due to the small asymmetry in the shock reflections caused by the slight mismatch in Mach numbers entering the test section on either side of the jet nozzle.

This slight asymmetry in the shock pattern can be seen in Fig. 9, which shows a typical shadowgraph image of the flow. The mean PLMS image from Fig. 8 is superimposed for comparison. The wake shock curves just before and after the first reflection from the sidewalls due to interaction with the expansion fan and its reflection. Figure 10 shows the static pressure distribution measured along both sidewalls, where the effect of the slight asymmetry in the wave pattern is evident.

Lateral profiles of the relative intensity at various downstream locations in the mean PLMS image in Fig. 8 are shown in Fig. 11. The downstream growth of the wake is evident in these profiles, which are used in §5.1 to compare the growth of the supersonic wake with results for incompressible wakes.

3.3 Near-Wake Region

Instantaneous shadowgraph and PLMS images of the base flow and near-wake regions are shown in Figs. 12 and 13. As noted above, the PLMS images correspond to a small volume flow rate. No evidence of "eddy shocklets" of the type seen by Clemens *et al* (1996) and Clemens & Smith (1998) in slender body wakes is found in these shadowgraph images of the bluff-body wake. In the PLMS images in Fig. 13, it is apparent that no quasi-periodic, large scale, organized structures have formed over the imaged region of the flow.

3.4 Near- to Far-Wake Transition Region

Figure 14 shows instantaneous shadowgraph and PLMS images covering the transition region from the base flow into the far-wake region. The right hand edge is at x = 5.6 cm, corresponding to $(x/\vartheta) = 140$. The development of organized, vortex street-like structures is apparent in the center panel, however no "eddy shocklets" associated with these large-scale structures are apparent in the top panel.

Also shown in the bottom panel are measured profiles of pitot pressure at eight downstream locations spanning this transition region. These are superimposed on a shadowgraph image, allowing the wave structure to be reconciled with the pressure profiles. The extent of the expansion fan and the point where the trailing Mach wave intersects the recompression shock can be readily seen.

4. SIMILARITY SCALING

4.1 Similarity Profiles

The mean pitot pressure profiles at the eight downstream locations in Fig. 14 were each converted to mean velocity profiles $U(y)$, and subsequently to mean velocity defect profiles

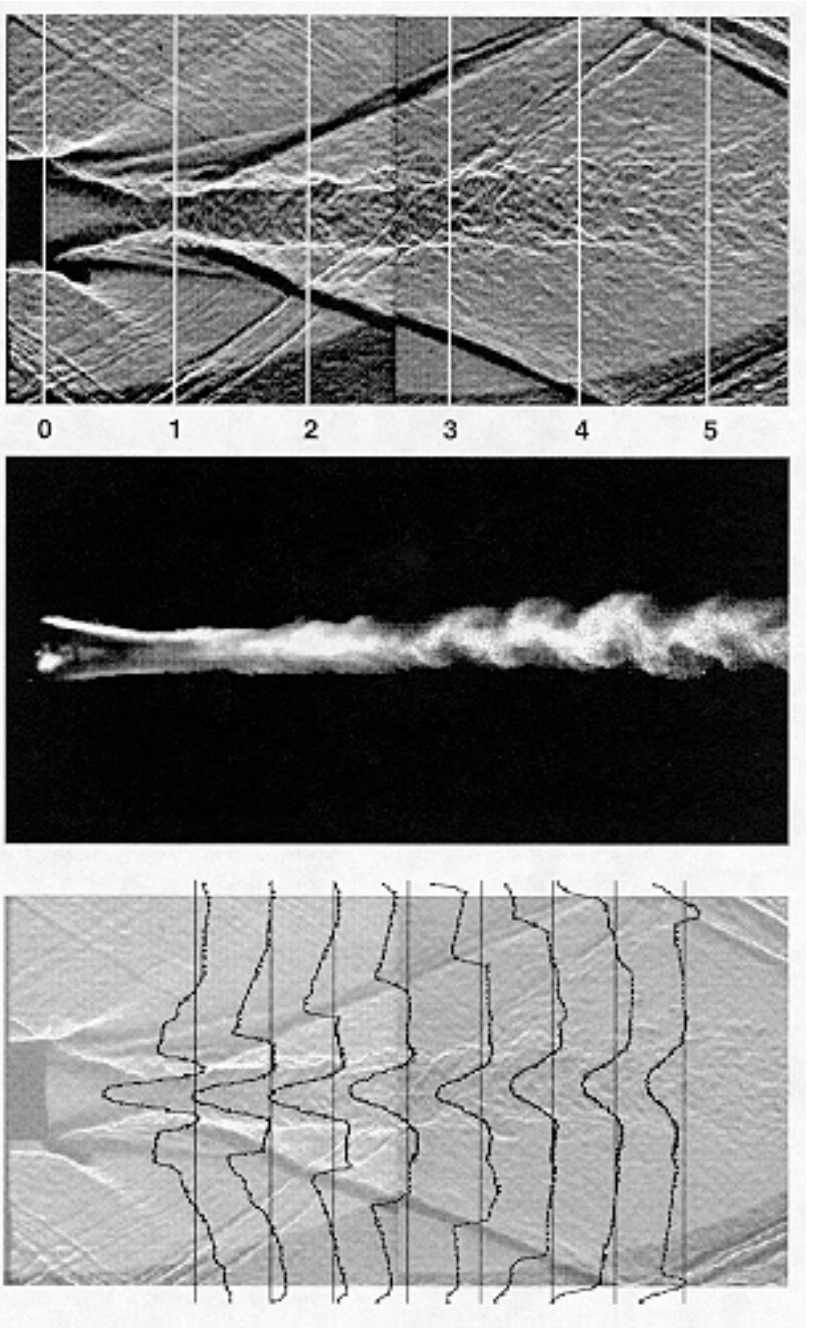

Figure 14. Transition region from near-field to far-field wake, showing typical shadowgraph image *(top)*, typical instantaneous PLMS image *(middle)*, and measured total pressure profiles superimposed on shadowgraph image *(bottom)*.

$u(y) \equiv U_\infty - U(y)$. A Gaussian fit was determined for each $u(y)$ profile by matching the three lowest moments over the central portion of the flow spanning across the wake, allowing the local centerline location $y_0(x)$, local centerline velocity $u_0(x)$, and local flow width $\delta_{1/2}(x)$ of each profile to be found. Here $\delta_{1/2}$ denotes the half-width at the half-maximum point of the local mean velocity defect profile.

Each of the measured velocity defect profiles $u(y)$, normalized by the local centerline velocity $u_0(x)$, with y centered on $y_0(x)$ and normalized by $\delta_{1/2}(x)$, is shown in Fig. 15. It is apparent that, except for the furthest upstream profile at x = 1.17 cm [corresponding to $(x/\vartheta) = 29$], all of the mean velocity defect profiles are very nearly self-similar for $(x/\vartheta) = 43$ and beyond.

The local wake momentum thicknesses $\vartheta(x)$ determined by appropriately integrating each of these $u(y)$ profiles gives essentially the same result, namely $\vartheta(x) = 0.40 \pm 0.03$, at each of these downstream locations. Note that the furthest downstream location is well upstream of the first reflected shock

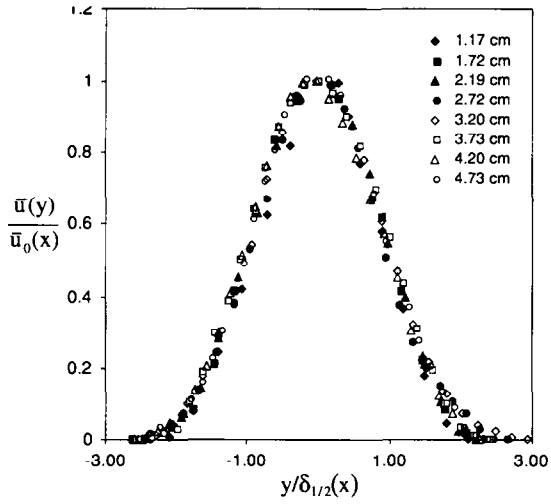

Figure 15. Similarity of measured mean velocity profiles, showing good collapse of all profiles except at the furthest upstream location.

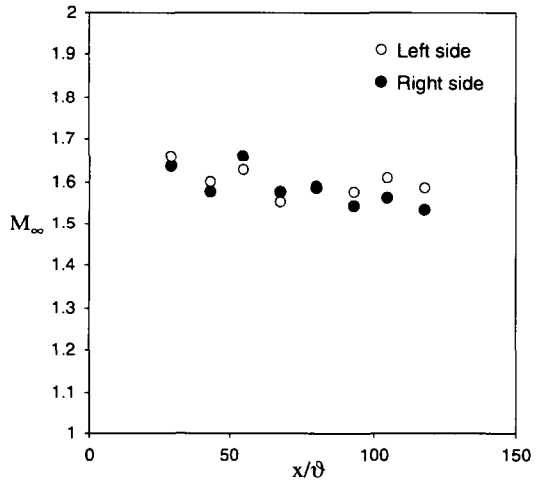

Figure 16. Free stream Mach number $M_\infty(x)$ outside the wake.

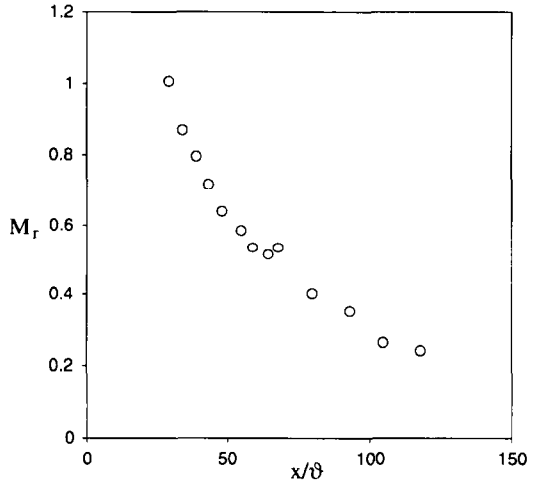

Figure 17. Relative Mach number $M_r(x)$ from pressure ratio measured on centerline at various downstream locations.

interaction with the wake.

4.2 Relative Mach Number $M_r(x)$

Unlike the mixing layer or the wake created by a thin splitter plate, which do not produce strong waves, the bluff-body wake inherently produces a corner expansion wave and recompression shock. Reflections of these waves from the tunnel sidewalls thus inherently lead to Mach number variations in the free stream, and a single "free stream Mach number M_∞" can thus not be defined.

Figure 16 shows the resulting free stream Mach numbers $M_\infty(x)$ immediately outside the flow on either side of the wake, determined from the measured pitot pressure profiles in Fig. 14 and the static pressure measured on the wake centerline. The Mach number entering the test section on either side of the slot nozzle was $M_\infty = 1.55$ and 1.59. These increase to 1.63 and 1.66, respectively, at the location of the first profile in Fig. 14, where the free streams have passed through expansion fan and recompression shock. Thereafter $M_\infty(x)$ gradually decreases to 1.53 and 1.59 at the furthest downstream location, namely x = 4.75 cm or $(x/\vartheta) = 118$.

The relative Mach number $M_r(x) \equiv u_0(x)/a_\infty$ determined by the mean centerline velocity defect serves a corresponding role in the supersonic wake as does the convective Mach number M_c in the supersonic mixing layer. Moreover unlike the mixing layer, for which M_c does not vary with downstream distance x, in the wake the velocity defect must decrease with increasing x, and thus the relative Mach number $M_r(x)$ must also decrease with x.

Figure 17 shows the resulting relative Mach number M_r at each location (x/ϑ), from the measured centerline velocity defects $u_0(x)$ in Fig. 15 and $M_\infty(x)$ in Fig. 16. It is apparent that $M_r(x)$ decreases rapidly, and that most of the far wake in Figs. 7 and 8 is at essentially incompressible local flow conditions. However in the supersonic turbulent mixing layer, reductions in the layer growth rate $d\delta/dx$ of more than 20% relative to the incompressible mixing layer are observed even at convective Mach numbers as low as 0.2. This suggests that, if observations in supersonic mixing layers are indeed indicative of generic effects of compressibility in other turbulent shear flows, then Fig. 17 would imply that measurable compressibility effects should be expected up to at least $(x/\vartheta) = 150$. This corresponds to slightly beyond the right hand edge of the images in Fig. 14.

5. INCOMPRESSIBLE WAKE COMPARISONS

To look for effects of compressibility in the supersonic wake analogous to those observed in supersonic turbulent mixing layers, we compare the local outer variable scalings $\delta_{1/2}(x)$ and $u_0(x)$ to corresponding results from incompressible, planar, turbulent wakes. These outer variable scalings determine the local entrainment rate into the turbulent wake, and since at large values of the local outer-scale Reynolds number $Re_\delta(x) \equiv u_0(x) \cdot \delta_{1/2}(x)/\nu$ the molecular mixing rate is entrainment-limited, these scalings also determine the mixing rate achieved by the flow.

In incompressible planar turbulent wakes, the outer variable scalings in the self-similar far field have been relatively well established (*e.g.*, Wygnanski *et al* 1986). In particular, the flow

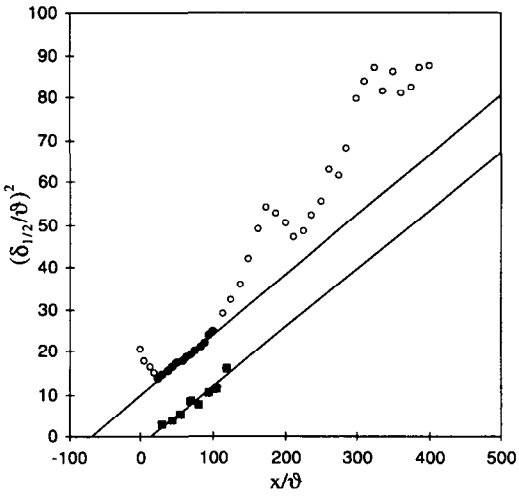

Figure 18. Measured flow width $\delta_{1/2}(x)$ from mean PLMS intensity profiles in Fig. 11 *(circles)* and from mean velocity profiles in Fig. 15 *(squares)*. Straight lines show $(\delta/\vartheta) \sim (x/\vartheta)^{1/2}$ scalings, and allow virtual origins and scaling constants to be determined. Accelerated growth rates near $(x/\vartheta) = 170$ and 300 coincide with locations of shock intersections in Fig. 9, indicated by arrows.

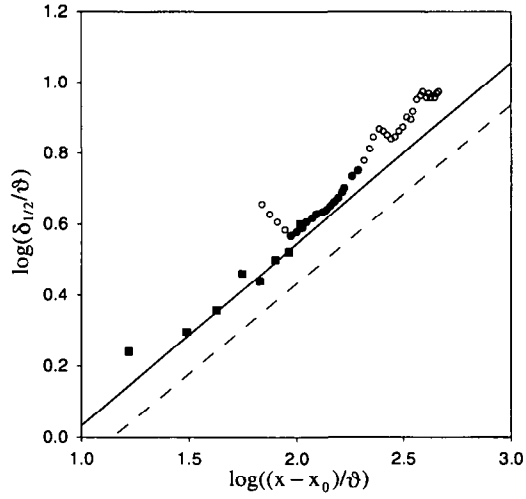

Figure 19. Flow widths $\delta_{1/2}(x)$ from Fig. 18 in log-log form, with lines indicating 1/2-power law scaling for values of the far-field scaling constant c_δ in (1) for unforced incompressible wakes *(dashed line)* and forced incompressible wakes *(solid line)* of Wygnanski *et al* (1986).

width scales with the wake momentum thickness as

$$(\delta_{1/2}/\vartheta) = c_\delta[(x-x_0)/\vartheta]^{1/2}, \quad (1)$$

and the centerline velocity defect scales as

$$(u/U_\infty) = c_u[(x-x_0)/\vartheta]^{-1/2}. \quad (2)$$

The scaling constants c_δ and c_u, and the virtual origin x_0, depend on the wake generator. For bluff-body wakes, Wygnanski *et al* (1986) find

$$c_\delta = 0.270 \quad (3a)$$

$$c_u = 1.88 \quad (3b)$$

and

$$(x_0/\vartheta) = -128. \quad (4)$$

For later reference, various other steady wake generators give $c_\delta = 0.29 \pm 0.03$ and $c_u = 1.70 \pm 0.2$. It is of interest to compare these power-law scalings and the constants for incompressible wakes with the present results for the supersonic wake.

5.1 Flow Width Scaling $\delta(x)$

In view of the incompressible scalings above, Fig. 18 shows $(\delta_{1/2}/\vartheta)^2$ plotted against (x/ϑ), with circles (closed and open) denoting the visual thickness $\delta_{1/2}(x)$ determined from moments of the lateral profiles through the mean PLMS image in Fig. 8, and with squares denoting $\delta_{1/2}(x)$ determined from the mean velocity defect profiles in Fig. 15. If the present supersonic wake follows the same $(x/\vartheta)^{1/2}$ power law scaling as does its incompressible counterpart, then the symbols in Fig. 18 should fall on straight lines, with the slopes being related to the scaling constant c_δ, and the virtual origin (x_0/ϑ) being identifiable by the x-intercept.

It is apparent from the squares in Fig. 18 that the flow widths $\delta_{1/2}(x)$ determined from the measured velocity defect profiles $u(y)$ obey the 1/2-power law scaling. At these comparatively small values of (x/ϑ), the relative Mach number $M_r(x)$ in Fig. 17 is large enough that any effects of compressibility should be apparent. The fact that the scaling exponent in Fig. 18 appears unchanged by compressibility may not be surprising based on experience in the supersonic mixing layer, where compressibility does not affect the power-law scaling, but reduces the scaling constant dramatically when $M_c > 0.2$.

Regarding the virtual origin in the compressible wake scaling, the squares in Fig. 18 give

$$(x_0/\vartheta) = +13. \quad (5)$$

This apparent downstream shift of the virtual origin relative to the incompressible value of -128 in (4) is not unexpected, given the reduction in wake width created by the expansion and recompression process in the base flow region in Fig. 12. Figure 5 suggests that the virtual origin would be expected to shift upstream (become more negative) with increasing jet flow rate. At sufficiently high flow rates, (x_0/ϑ) may approach the incompressible value.

The squares in Fig. 18 furthermore indicate the scaling constant in the flow width scaling to be

$$c_\delta = 0.38. \quad (6)$$

This is remarkable in that it is *higher* than the value in the incompressible wake in (3*a*), whereas experience in the supersonic mixing layer indicates a *reduction* in the value of the

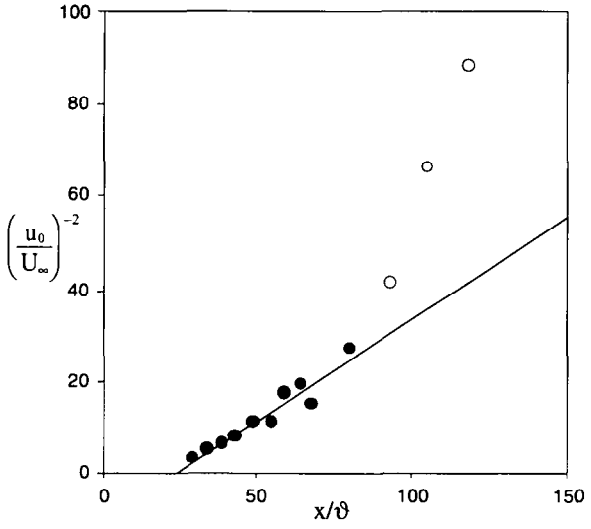

Figure 20. Wake centerline defect velocity $u_0(x)$ from velocity profiles in Fig. 15 obtained from pressure profiles in Fig. 14. Sraight line indicates $(u_0/U_\infty) \sim (x/\vartheta)^{-1/2}$ scaling, allowing virtual origin and scaling constant to be determined.

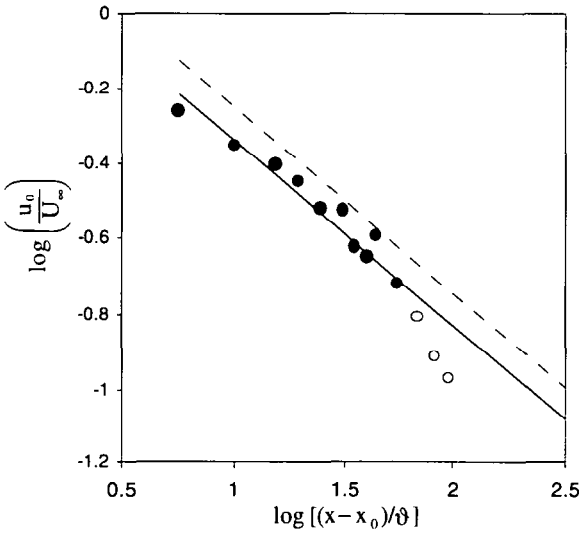

Figure 21. Wake centerline defect velocity $u_0(x)$ from Fig. 20 in log-log form, with lines indicating −1/2-power law scaling for values of the scaling constant c_u in (2) for the unforced incompressible wakes *(dashed line)* and forced incompressible wakes *(solid line)* of Wygnanski *et al* (1986).

flow width scaling constant due to compressibility effects. However a more appropriate interpretation of the result from the mixing layer may be that compressibility acts to reduce the *entrainment rate*, not the growth rate. In the mixing layer these two rates are directly proportional, but in most turbulent shear flows the entrainment rate depends on both the growth rate and the velocity defect decay rate. The latter will be examined in §5.2.

While the scaling constant c_δ from the squares in Fig. 18 is significantly higher than the value found for any *steady* wake generator by Wygnanski *et al* (1986), they found that periodic forcing introduced at the wake generator can dramatically increase the scaling constant over the value obtained from the same generator without forcing (see their Table 2). For forced wakes they find

$$c_\delta = 0.35 \pm 0.03, \qquad (7)$$

which would appear to be in accord with the present value in (6). It will be seen below that there is a strong likelihood that confined supersonic wakes, such as the present, experience shock-induced periodic forcing due to intersections of the reflected wake recompression shock with the organized vortical structure of the flow.

The circles in Fig. 18 represent the flow widths $\delta_{1/2}(x)$ determined from the mean PLMS profiles in Fig. 11. The first four points are within the base flow region where, as expected, the profile widths decrease with x due to the narrowing effect of the expansion and recompression process evident in Fig. 12. Beyond the recompression zone, the wake widths for the next ten points, indicated by solid circles, again increase in accordance with the $(x/\vartheta)^{1/2}$ power-law scaling noted above, as is evident from the straight line fit to these points. Moreover the slope of this line is the same as that for the squares, indicating the *same* value for the scaling constant, namely $c_\delta = 0.38$ as in (6). Only the virtual origin is different in this case, giving

$$(x_0/\vartheta)_{vis} = -70. \qquad (8)$$

As noted above, the downstream shift of the virtual origin relative to the incompressible value of −128 is not surprising. The fact that the virtual origin in (8) for the visual widths is more negative than that in (5) for the velocity profile widths appears to be consistent with the common observation that scalar profiles tend to be wider than velocity profiles in turbulent shear flow.

For $(x/\vartheta) \geq 110$, the data in Fig. 18 no longer appear to follow the $(x/\vartheta)^{1/2}$ power-law scaling of the incompressible wake. Yet these far downstream locations are precisely where the relative Mach number in Fig. 17 has decreased to essentially incompressible values. To understand this, it is essential to note that the circles in Fig. 18 show two strong peaks centered roughly at $(x/\vartheta) \approx 170$ and 325, corresponding respectively to x = 6.8 cm and 13.0 cm. These positions coincide with the dark regions in Fig. 8, which in turn coincide with the locations where the reflected recompression shocks intersect the wake flow.

This suggests that the rapid increase and subsequent decrease in the flow width in Fig. 18 at these locations may be a result of sympathetic interactions between the reflected shock waves and the quasi-periodic, large-scale, vortical structure of the wake evident in Fig. 7. A similar phenomenon is commonly observed in periodically forced mixing layers (*e.g.*, Oster & Wygnanski 1982). At downstream locations where the forcing frequency closely matches the local natural frequency $u(x)/\delta(x)$ associated with the passing of large-scale structures in the flow, the vortical structures lock onto the forcing frequency. This effect causes the flow width to increase much more rapidly than it normally

would as it approaches the point where the natural frequency and the forcing frequency match, and then to remain locked at roughly that width for some distance past this point, before subsequently returning to its natural growth rate.

In the supersonic wake, such periodic forcing could result from the passing of the organized large-scale vortical structures in the wake flow through the reflected wake shocks in Fig. 9. As a consequence of this inherently quasi-periodic forcing mechanism, the resulting local forcing frequency would automatically be matched to the local natural frequency of the vortical structures, irrespective of where the shocks intersect the flow. While the supersonic mean flow Mach number might appear to preclude upstream propagation of disturbances from this local forcing, any subsonic path in the instantaneous Mach number field would allow such propagation. Thus the frequency locking phenomenon previously documented in incompressible mixing layers could occur at both downstream locations where the reflected shock waves pass through the wake. After the first intersection, the flow begins to return to its natural growth, given by the line in Fig. 18, but before reaching this the second interaction occurs and causes the locking process to repeat. It is presumably this mechanism that causes the circles in Fig. 18 to depart from the incompressible scaling, given by the line, at downstream distances for which the relative Mach number $M_r(x)$ has decreased to clearly incompressible values.

This suggests that in the absence of shock reflections, as would be the case in an unconfined wake, the circles in Fig. 18 would have continued to follow the unforced growth rate given by the line, namely

$$(\delta_{1/2}/\vartheta) = 0.38\,[(x-x_0)/\vartheta]^{1/2}. \qquad (9)$$

Moreover, the shock-induced periodic forcing of the wake noted above appears to reconcile the value of the scaling constant c_δ in (6) for the present supersonic wake with the results in (7) of Wygnanski *et al* (1986) for periodically-forced incompressible wakes. This would, furthermore, suggest a mechanism for potentially *increasing* the growth rates of supersonic turbulent shear flows through judicious use of such shock wave interactions with the flow. The comparatively strong large-scale structures in two-dimensional, supersonic, turbulent wakes and mixing layers may make these flows particularly suited for such mixing enhancement by self-induced frequency locking of their vortical structures.

Figure 19 shows the mean flow width scaling, in log-log form, with the appropriate value of the virtual origin for the data in Fig. 18. Also shown for comparison are the unforced and forced incompressible wake scalings of Wygnanski *et al* (1986).

The results in this section, as summarized in Fig. 19, collectively suggest that the effect of compressibility on the flow width scaling $\delta(x)$ of supersonic, planar, turbulent, bluff-body wakes is *(i)* no change in the exponent of the power-law scaling, *(ii)* a downstream shift in the virtual origin due to the expansion and recompression in the base flow region, the magnitude of which depends on the jet flow rate into this region, and *(iii)* in the case of confined wakes, an increase in the scaling constant from its unforced value in incompressible wakes to a somewhat higher value consistent with forced incompressible wakes, due to sympathetic interactions between the vortical structures in the wake and reflected shocks passing through the flow.

5.2 Velocity Defect Scaling $u(x)$

Based on the scaling in (2) for decay of the mean velocity defect in incompressible turbulent wakes noted above, Fig. 20 shows $(u_0/U_\infty)^{-2}$ plotted against (x/ϑ), where the centerline velocities are determined from measured pitot and static pressures. If the supersonic wake follows the same $(x/\vartheta)^{-1/2}$ power law scaling as does the incompressible wake, then the symbols in Fig. 20 should fall on straight lines, with the slope determining the scaling constant c_u and the virtual origin (x_0/ϑ) identified by the x-intercept.

Over roughly the same downstream region where the flow widths in Fig. 18 follow the incompressible scaling, it is again apparent that the centerline velocity defect also follows the $-1/2$ power-law scaling of the incompressible wake, as indicated by the line in Fig. 20. The virtual origin in this case is found to be

$$(x_0/\vartheta) = +24, \qquad (10)$$

in reasonable agreement with the value obtained for the velocity profile widths in (6) from Fig. 18.

The slope of the line in Fig. 20 corresponds to a value for the scaling constant of

$$c_u = 1.51\,. \qquad (11)$$

This is somewhat lower than the value of 1.88 in (3*b*) found by Wygnanski *et al* (1986) for unforced, incompressible, bluff-body wakes. However, as noted above, intersections of the reflected wake recompression shock with the flow appear to produce periodic forcing of the vortical structures in the wake, and consequently the value for c_u in (11) from Fig. 20 should be compared with results for periodically forced wakes of Wygnanski *et al*. Indeed their Table 2 shows that forcing acts to reduce the value of c_u, in accordance with the result in (11). In their results the average reduction gives

$$c_u \approx 1.46 \pm 0.1, \qquad (12)$$

which is reasonably close to what was found here.

The higher velocity decay rate demonstrated by the three farthest downstream points in Fig. 20 presumably reflects the increased growth rate caused by incipient locking of the vortical structures onto the forcing frequency produced by the first shock intersection with the wake. In the absence of the vortex locking mechanism, these points would have continued to follow the forced growth rate given by the line, namely

$$(u/U_\infty) = 1.51\,[(x-x_0)/\vartheta]^{-1/2}. \qquad (13)$$

From (9) and (13), the outer-scale Reynolds number $Re_\delta(x)$ is independent of x and equal to $Re_\vartheta \cdot c_\delta\, c_u$, where Re_ϑ is the Reynolds number based on momentum thickness ϑ and the free stream velocity. The present U_∞ = 450 m/s and ϑ = 0.40 mm give $Re_\vartheta \approx$ 14,000.

Figure 21 shows the centerline mean velocity defect scaling in (13), in log-log form, for the supersonic turbulent wake. Also shown are the unforced and forced scalings of Wygnanski *et al* (1986) for comparison. As this figure shows, the effect of compressibility on the velocity decay scaling of supersonic, planar, turbulent, bluff-body wakes is: *(i)* no change in the

exponent of the power-law scaling, *(ii)* the same downstream shift in the virtual origin due to the base flow region and depending on the jet flow rate into the base region, and *(iii)* when shock waves intersect the flow, a decrease in the scaling constant from its unforced value in incompressible wakes to a somewhat lower value consistent with forced incompressible wakes.

6. CONCLUSIONS

Major observations from the present experimental study of compressibility effects on entrainment and mixing in the near- and far-fields of a supersonic, planar, turbulent, bluff-body wake include the following:

1. The classical vortex street-like large-scale structure of incompressible, planar, turbulent wakes is recovered in the far field of the present supersonic wake.

2. These vortical structures become apparent around $(x/\vartheta) \approx 75$ in the present experiments, where the relative Mach number $M_r(x)$ has decreased to around 0.4.

3. A classical supersonic base flow region exists immediately past the jet exit. The jet flow rate into this base flow affects its size and alters the expansion fan and recompression shock. This also appears to affect the virtual origin (x_0/ϑ) in the far-field similarity scalings.

4. Mean velocity profiles in the present experiments have become self-similar by $(x/\vartheta) \approx 43$.

5. The flow width and mean centerline velocity defect follow the classical $(x/\vartheta)^{1/2}$ and $(x/\vartheta)^{-1/2}$ scalings characteristic of incompressible, planar, turbulent wakes.

6. In supersonic wakes, the virtual origin (x_0/ϑ) in these far field scalings is shifted downstream by the wake pinching that occurs in the base flow region.

7. The measured scaling constants c_δ and c_μ in these far field scalings differ significantly from accepted values for unforced, incompressible, planar, turbulent wakes, but agree well with corresponding values for periodically forced incompressible wakes.

8. The local growth rate of the wake is dramatically higher in the downstream regions where the reflected recompression shocks intersect the flow.

9. The enhanced growth rate near the shock intersections may be attributable to a possible quasi-periodic forcing mechanism that results from passage of the organized large-scale vortical structures through the shock waves. The response of the wake to this local forcing mechanism appears analogous to the response of incompressible mixing layers to periodic forcing. This suggests that such shock wave interactions may be a potentially useful means for enhancing the natural growth of supersonic turbulent wakes.

Collectively these results suggests that, while certain conclusions regarding compressibility effects on turbulent mixing drawn from studies of supersonic turbulent mixing layers can be applied to other flows, many of the major effects of compressibility observed in other turbulent shear flows cannot be anticipated from experience in the mixing layer. Moreover, the present study of the supersonic turbulent wake indicates a potential mechanism by which the natural growth rate and other processes intimately connected with entrainment and mixing in the supersonic flow can be altered through sympathetic interactions between shock waves and the large-scale vortical structures of the flow.

Acknowledgements

This work has been supported by the Air Force Office of Scientific Research under AFOSR Grant Nos. F49620-95-1-0115 and F49620-98-1-0003.

References

Amatucci, V.A., Dutton, J.C., Kuntz, D.W. & Addy, A.L. (1992) Two-stream, supersonic, wake flowfield behind a thick base. Part I: General features. *AIAA J.* **30**, 2039-2046.

Berger, S.A. (1971) Laminar Wakes. Elsevier, New York.

Chapman, D.R. (1951) An analysis of base pressure at supersonic velocities and comparison with experiment. NACA TN-2137, National Advisory Committee on Aeronautics.

Chen, J.H., Cantwell, B.J. & Mansour, N.N. (1990) The effect of Mach number on the stability of a plane turbulent wake. *Phys. Fluids A* **2**, 984-1004.

Clemens, N.T., Smith, M.F. & Fernandez, J.V. (1996) Observations of supersonic flat plate wake transition. *AIAA Paper No. 96-0785*, 34th Aerospace Sciences Meeting, AIAA, Washington, D.C.

Clemens, N.T. & Smith, M.F. (1998) Observations of supersonic flate plate wake transition. *AIAA J* **36**, 1328-1330.

Crookson, R.A., Flanagan, P. and Penny, G.S. (1969) A study of free-jet and enclosed supersonic diffusion flames. *Proc. 12th Int'l Symp. Comb.* 1115-1124, The Combustion Institute, Pittsburgh.

Dimotakis, P.E. (1991) Turbulent free shear layer mixing and combustion. In High-Speed Flight Propulsion Systems (S.N.B. Murthy & E.T. Curran, Eds.) Vol. 137 of Progress in Aeronautics & Astronautics, AIAA, Washington, D.C., pp. 265-340.

Herrin, J.L. & Dutton, J.C. (1994) Supersonic base flow experiments in the near wake of a cylindrical afterbody. *AIAA J.* **32**, 77-83.

Lachney, E.R. & Clemens, N.T. (1998) PLIF imaging of mean temperature and pressure in a supersonic bluff wake. *Expts. Fluids* **24**, 354-363.

Lachney, E.R., Smith, M.F. & Clemens, N.T. (1995) Laser 2-D imaging of a compressible flat plate wake. *AIAA Paper No. 95-2220*, 26th AIAA Fluid Dynamics Conference, AIAA, Washington, D.C.

Nejad, A.S., Glawe, D.D., Donbar, J.M., Sekar, B, Samimy, M. & Driscoll, J.F. (1994) Parallel fuel injection from the base

of an extended strut into supersonic flow; *AIAA Paper No. 94-0711*, AIAA, Washington, D.C.

Northam, G.B., Greenburg, I. & Byington, C.S. (1989) Evaluation of parallel injector configurations for supersonic combustion. *AIAA Paper No. 89-2525*, AIAA, Washington D.C.

Oster, D. & Wygnanski, I. (1982) The forced mixing layer between parallel streams. *J. Fluid Mech.* **123**, 91-130.

Pope, A. & Goin, K.L. (1965) High-Speed Wind Tunnel Testing. John Wiley & Sons, New York.

Wygnanski, I., Champagne, F. & Marasli, B. (1986) On the large-scale structures in two-dimensional, small-deficit, turbulent wakes. *J. Fluid Mech.* **168**, 31-71.